Local Structure of v Dopants in TiO2 Nanoparticles: X-ray Absorption Spectroscopy, Including Ab-Initio and Full Potential Simulations

(Article begins on next page)

Local Structure of V Dopants in TiO$_2$ Nanoparticles: X-Ray Absorption Spectroscopy, Including Ab-Initio and Full Potential Simulations

Giacomo Rossi, Marco Calizzi, Valeria Di Cintio, Sotirios Magkos[§], Lucia Amidani[†], Luca Pasquini,

Federico Boscherini[*]

Department of Physics and Astronomy, University of Bologna

Viale C. Berti Pichat 6/2, 40127 Bologna, Italy

[§] Also at: Department of Physics, Aristotle University of Thessaloniki, Greece

[†] Present address: ESRF – The European Synchrotron, Grenoble, France

[*] Corresponding author. E-mail: federico.boscherini@unibo.it

ABSTRACT

Doping with transition metals is an effective method to enhance visible light absorption in TiO_2 nanoparticles and to improve the efficiency of many photocatalytic processes under solar radiation. A determination of the incorporation site of the dopant and an understanding of the local bonding arrangement and electronic structure is a necessary step for knowledge – based materials design. In this paper, we report an in-depth X-ray Absorption Spectroscopy study of V dopants in TiO_2 nanoparticles deposited by gas phase condensation with a local structure similar to anatase, rutile or intermediate. The combination of K and L edge spectra in the pre-edge, edge, and extended energy regions with full potential ab-initio spectral simulations shows that V ions occupy substitutional cationic sites in the TiO_2 structure, irrespective of whether it is similar to rutile, anatase or mixed.

INTRODUCTION

In recent years, titanium dioxide (TiO_2), especially in the form of nanoparticles (NPs), has become one of the most studied wide band gap oxide semiconductors due to its photocatalytic properties, which open the way to various applications such as hydrogen production from water, environmental cleaning (air and water), dye synthesized solar cells and others.[1] However, because of its wide band gap (≈ 3.2 and 3.0 eV in anatase and rutile polymorphs, respectively), only a small fraction of the solar spectrum, i.e. UV light (3-5% of total), can be used for photocatalytic processes. The incorporation of $3d$-transition metals in TiO_2 is an effective approach to decrease the band gap and to improve visible light photocatalytic activity.[2] Band gap reduction is the result of the creation of states in the band gap of the matrix, as systematically investigated theoretically by Umebayashi et al.[3] They found that V, Cr, Mn, Fe and Co create donor states, their position shifting towards the valence band with increasing atomic number; V, the subject of the present paper, was predicted to create a gap state near the bottom of the conduction band. Another route for band gap reduction is N – doping, which induces acceptor states above the valence band maximum.[4] Clearly, photocatalysis is due to more complex processes than just light absorption, many of which are crucially linked to dopant sites. In fact, dopants may induce charge carrier recombination or scattering (which lead to reduced efficiency) or may trap charge carriers for long time intervals near the surface of NPs, making them available for oxidation and reduction processes (leading to improved efficiency). Therefore, a detailed atomistic knowledge of the charge dynamics involving defect sites is of paramount importance for a physical understanding of the material's function and may lead to knowledge-based device engineering.

X-ray Absorption Spectroscopy (XAS) is a powerful tool to study the local atomic and electronic structure of condensed matter. Detailed analysis of the fine structure oscillations in an extended energy range (so – called EXAFS: Extended X-ray Absorption Fine Structure) based on the real – space multiple scattering (MS) formalism[5–7] is able to provide a quantitative determination of the composition of the

3

first few coordination shells around the excited atom, the interatomic distances and their spread around the average value. Moreover, analysis of the lineshape of the spectral region near the absorption edge (so – called XANES: X-ray Absorption Near Edge Structure) can provide important information on the oxidation state, valence, atomic geometry and site / symmetry selected density of states (DOS) of unoccupied electronic states. Simulations based on the MS formalism are also very useful for XANES interpretation and there are continuing improvements in methods to reproduce experimental data, for example using density functional electronic structure calculations and finite difference numerical methods,[8,9] which will be employed in the present investigation. It is possible to choose some experimental parameters in XAS experiments to provide flexibility and added value. By tuning the photon energy to the absorption edges of different elements their local structure can be independently studied; by using absorption edges due the excitation of electrons with different orbital angular momentum (s, p or d) and exploiting the dipole selection rule, various components of the unoccupied electronic DOS can be probed with different spectral weight; finally, by using shallower absorption edges, which are characterized by longer core hole lifetimes, sharper lineshapes can be obtained compared to those for more tightly bound ones in the hard X-rays (albeit with the complication of a high surface sensitivity).

Due to its local character, XAS is particularly useful to study disordered or defective atomic arrangements in condensed matter, such as those which are present in NPs.[10] Also very important for the present investigation, XAS is the premier structural tool to determine the incorporation site of dopants in condensed matter[11–13] since it is possible in many cases to isolate the XAS cross – section of the excited atom from the background contribution.

The K – edge absorption edges of transition metals exhibit characteristic "pre – edge" peaks, due to transitions to bound unoccupied states.[14] Their lineshape can in many cases provide important information on the oxidation state, valence and local geometry of the probed ion. In the specific case of

4

TiO$_2$ polymorphs these peaks are known to be due to dipole and quadrupole transitions to *p–d* hybridized orbitals split by the crystal field in two t_{2g} and e_g components.[9,15,16] We note that the full Ti *K*-edge XAS spectra (including pre-edge, XANES and EXAFS regions) of rutile and anatase have been reproduced quite well in an early attempt.[17]

The same two t_{2g} and e_g orbitals which give rise to the relatively weak Ti *K*-edge pre-edge peaks originate the main features of the $L_{2,3}$ edge XANES spectrum in TiO$_2$ polymorphs. We note that the transitions from *p* core levels to the *d* component of the final states are dipole allowed; the $L_{2,3}$ edge spectra can be interpreted by crystal field multiplet calculations taking account the effects of local distortions which eliminate the degeneracy of the t_{2g} and e_g states.[18,19] As mentioned, these spectra exhibit an intrinsically high energy resolution. The same orbitals are also probed by O *K*-edge spectra;[20,21] in this case the spectra are dominated by transitions to the *p* component of the final states and they are poorer in spectral features compared to the Ti *L* ones.

XAS has been previously applied to materials systems based on TiO$_2$ NPs. In nanostructured TiO$_2$ the sensitivity of the Ti *K*-edge pre–edge peak lineshape to the degree of defectivity (specifically, to the amount of undercoordinated, five-fold, Ti sites) has been established.[20,22–25] Concomitant changes in the Ti $L_{2,3}$ edge and O *K*-edge XANES have been convincingly documented[20]. Some analyses of the EXAFS region of Ti *K*-edge in TiO$_2$ NPs have been reported,[21–24] although multiple scattering contributions have not been included in these studies.

There have been some previous XAFS studies of dopants in TiO$_2$ NPs. Li et al.[26] and Rodríguez-Torres et al.[27] have studied Nd and Fe doped anatase NPs, respectively. They found that Nd^{3+} and Fe^{3+} cations substitutionally replace Ti^{4+} ones in anatase NPs, with increased cation – oxygen first shell bond lengths. A recent study[28] of Nb dopants also supports a substitutional site. The present paper concerns V dopants, we thus note an early detailed study[29] of the pre – edge features in the V *K* – edge spectra of VO$_2$ across the metal – to – insulator transition at 68°C and systematic studies of the variation of the pre

– edge and XANES features in V compounds, minerals, basaltic and silicate glasses[30–32]. These papers demonstrate the dependence of spectral features on local coordination and oxidation state. In particular, with increasing oxidation state the energy of the pre – edge peak and its intensity clearly increase.

The incorporation of V in TiO_2 catalysts by impregnation by an acqueous solution has been studied using V K – edge XANES, including some *ab – initio* simulations, by Izumi et al.[33]; these authors claim a five – fold oxygen coordination for V, despite a limited agreement between experiment and simulation. V doping in anatase nanoparticles synthesized by hydrothermal decomposition of Ti and V peroxo – complexes has been studied by Avansi et al.[34], also using a preliminary qualitative analysis of V K – edge XANES and supporting a substitutional site; some indicative support for a substitutional site in V-doped anatase NPs obtained by solution combustion was reported by Nagaveni et al. [35], but no locally sensitive technique was employed in that paper. Finally, we note that XAS has been recently used to track light induced charge transfer processes in un-doped TiO_2 NPs.[36,37]

In this paper we report an in – depth study of V – doped TiO_2 NPs deposited by gas phase condensation. Using a combination of K and L edge XAS at the Ti and V edges and including Density Functional Theory (DFT) structural relaxations and *ab – initio* simulations of the V K-edge XANES spectra using full potential methods we study the local structure of Ti in the host matrix and of the V dopant. The local structure of the matrix was found to be similar to rutile, anatase or intermediate, depending on the deposition parameters. We demonstrate that V dopants occupy substitutional cationic sites, irrespective of the local structure of the matrix.

EXPERIMENTAL AND THEORETICAL METHODS

Sample preparation and characterization. V-doped TiO_2 nanoparticles were grown by gas-phase condensation in a vacuum chamber (base pressure $1x10^{-5}$ Pa) filled with 266 Pa of He (99.9999% pure)[38]. Ti powders (99.9 % purity, -50 mesh, Alfa Aesar) and V powders (99.5 % purity, -325 mesh, Alfa Aesar)

were gently mixed and loaded in a W boat for thermal evaporation. The Ti-V phase diagram[39] indicates complete miscibility above the temperature of 882 °C, which corresponds to the hcp→bcc structural transition in pure Ti. In order to obtain a Ti-V alloy precursor, the powder mixture was first heated under vacuum above the melting point of Ti (1668 °C), then rapidly cooled down to about 1200 °C where no measurable evaporation takes place, and left homogenize for 2 hours. Afterwards, He was admitted in the chamber in close proximity of the W boat at a flow rate of 65 mln/min. A stable He pressure in the chamber was maintained under dynamic conditions using a back rotary pump. The temperature of the W boat was slowly increased to attain the desired deposition rate, monitored by a quartz crystal microbalance (QCM). The He flow directed the NPs, which are formed by homogeneous nucleation in the gas phase, towards the collection substrates. After the deposition, high vacuum was restored in the chamber and finally the nanoparticles were oxidized by admitting 99.999% pure O_2 up to a final pressure of 2.6 kPa. For all XAS measurements, nanoparticle-assembled films were deposited on super-smooth (111) Si substrates (Agar scientific, surface finish roughness < 1 nm) at room temperature. The film thickness, determined by the calibrated QCM and checked by atomic force microscopy, was about 240 nm for all samples.

The V content in the samples was determined by energy dispersive X-ray spectroscopy (EDX) in a Cambridge Stereoscan 360 Scanning Electron Microscope (SEM). Typically, the V content in the samples was about 4 times lower than in the precursor alloy, due the lower vapor pressure of V compared to Ti in the Ti-V alloy. In the following, the V content will be given by an atomic percentage (at. %), obtained dividing the number of V atoms by the total number of Ti plus V atoms (i.e., not counting O atoms). For instance, 4 at.% V corresponds to an overall composition of $Ti_{0.96}V_{0.04}O_2$.

The as-deposited samples were structurally amorphous and became crystalline after annealing in air at sufficiently high temperature. The structural evolution of a sample with 8 at.% V after an annealing time of 6 hours at different temperatures is shown by the X-ray diffraction (XRD) patterns in Figure 1.

XRD data were collected using a Panalytical X'Celerator powder diffractometer. Bragg reflections of anatase (a) and rutile (r) TiO_2 began to appear after annealing 300 °C, while full crystallization was induced by annealing at 400 °C. Notice that for XRD measurements, nanoparticles were deposited on a large stainless steel cylinder cooled by liquid nitrogen, allowing for the collection of a suitable amount of nanopowders (10-100 mg). In the XRD patterns, Bragg reflections attributable to vanadium oxides were not detected.
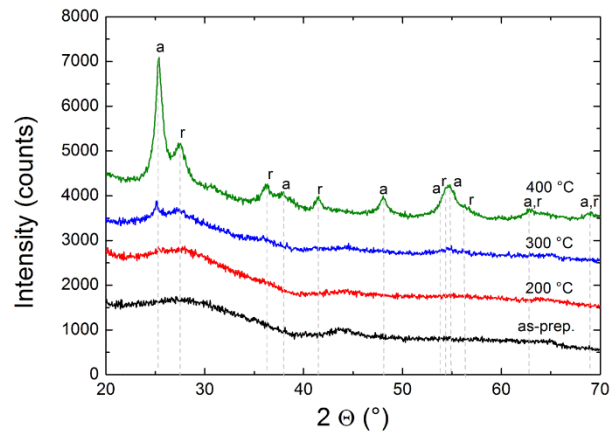
Figure 1: XRD patterns of a nanopowder sample with 8 at.% V subjected to 6 hours annealing at different temperatures. The Bragg reflections of anatase (a) and rutile (r) TiO_2 are indicated. The different patterns are vertically shifted for the sake of clarity.

Based on the above results, crystalline samples for XAS measurements were prepared by annealing the as-deposited nanoparticle-assembled films in the 350-400 °C range. Table 1 summarizes the main characteristics of the investigated samples, in terms of V content, deposition rate, and annealing treatment.

Table 1: Summary of sample characteristics and types of XAS measurements performed at Ti and V edges. Samples numbered from 1 to 8 are the V-doped TiO_2 nanoparticles-assembled films, for which V content, deposition rate, and annealing treatment are specified; all annealing times are 15 hours. The remaining samples are commercial reference materials.

sample	V/(V+Ti) (at.%)	deposition rate (nm/min)	description	Ti edges	V edges
m	–	–	Ti metal reference	K – edge XANES and EXAFS	–
a	–	–	anatase reference	K – edge XANES and EXAFS	–
r	–	–	rutile reference	K – edge XANES and EXAFS	–
1	3.5 ± 1.0	1.4	as - deposited	K – edge XANES	K – edge XANES
2	3.5 ± 1.0	1.4	annealed at 400 °C	K – edge XANES and EXAFS	K – edge XANES
3	4.4 ± 1.1	1.9	as - deposited	K – edge XANES	K – edge XANES
4	4.4 ± 1.1	1.9	annealed at 350 °C	K – edge XANES and EXAFS	K – edge XANES
5	4.4 ± 1.1	1.9	annealed at 400 °C	K – edge XANES and EXAFS	K – edge XANES
6	7.5 ± 0.9	1.6	annealed at 400 °C	K – edge XANES and EXAFS	K – edge XANES
7	8.0 ± 1.2	1.6	as - deposited	$L_{2,3}$ edges	L2,3 edge XANES
8	8.0 ± 1.2	1.6	annealed at 400 °C	$L_{2,3}$ edges	L2,3 edge XANES
V_2O_5	–	–	reference	–	K – edge XANES
VO_2	–	–	reference	–	K – edge XANES
V_2O_3	–	–	reference	–	K – edge XANES

Crystallization was accompanied by a marked change in the color of the samples: Nanopowders turned from nearly black to orange, while films deposited on glass gained a yellowish transparency. In order to assess the effect of V-doping on the optical properties of crystalline V-TiO_2, we measured UV-

vis Diffuse Reflectance (DR) spectra. For these experiments, we used a small amount of nanopowder, scraped from the substrate holder after evaporation and annealed under the same conditions as the nanoparticle-assembled films. The DR spectra were collected by a Perkin-Elmer Lambda 45 double beam spectrophotometer equipped with a RSA-PE-20 integrating accessory (Labsphere). The samples were measured as solid mixtures in a matrix of ground NaCl. Prior to measurement, a blank of pure NaCl was recorded as a reference. To test the suitability of NaCl for its employment in the UV region, a spectrum of the blank was recorded against the $BaSO_4$ reference (100 %R) and did not show any strong absorption band in the investigated interval, thus assessing the reliability of the measurement in the interval 200-1100 nm. DR spectra were converted into absorbance by the Kubelka-Munk function and the band gap of the samples was estimated by applying the Tauc method[40]. Figure 2 displays the absorbance of V-doped crystalline samples compared to an undoped sample, which was prepared under the same conditions of sample 2 using pure Ti as precursor. Figure 2 shows that V-doping induces a shift of the absorption band edge toward longer wavelengths. In addition, V-doped samples exhibit an absorption tail that extends above 500 nm. These two features are very similar in samples 2 and 5 with a similar V content, while they are stronger for sample 6 with the highest V-doping. Accordingly, the Tauc analysis yields a band gap of 3.18(3) eV for the undoped sample, 2.98(3) eV for sample 2, 3.01(3) eV for sample 5, and 2.81(3) eV for sample 6. The V-induced shift of optical absorption features toward the visible light region fully agrees with previous studies,[2,34,41–43] which attribute it to V incorporation in the TiO_2 structure.
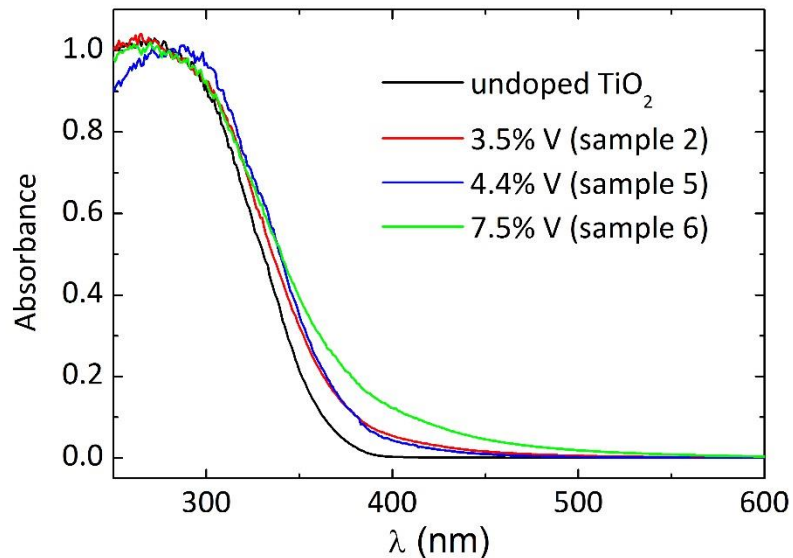
Figure 2: UV-vis absorbance of V-doped and undoped TiO$_2$ NPs, obtained by applying the Kubelka-Munk function to DR spectra and normalized to unit value at 280 nm

The morphology of both as-deposited and crystalline nanoparticle-assembled films was examined by a Zeiss Gemini 1530 Field Emission SEM (FESEM). Figure 3 displays the morphology of samples 2 and 5 at different magnifications. The NPs assemble in large agglomerates with a size of several tens of nanometers. Primary NPs with a typical diameter in the 10-20 nm range can be easily recognized within the agglomerates. Sample 5, deposited at 1.9 nm/min, exhibits a larger NP size compared to sample 2, deposited at 1.4 nm/min. This suggests that the NP size coarsens with increasing evaporation/deposition rate, a phenomenon commonly observed in gas-phase condensation.[44] The NP size influences the relative anatase / rutile phase abundance, as it will be shown in the next sections. FESEM also revealed that annealing at 400 °C did not induce any significant coarsening of the nanoparticles.
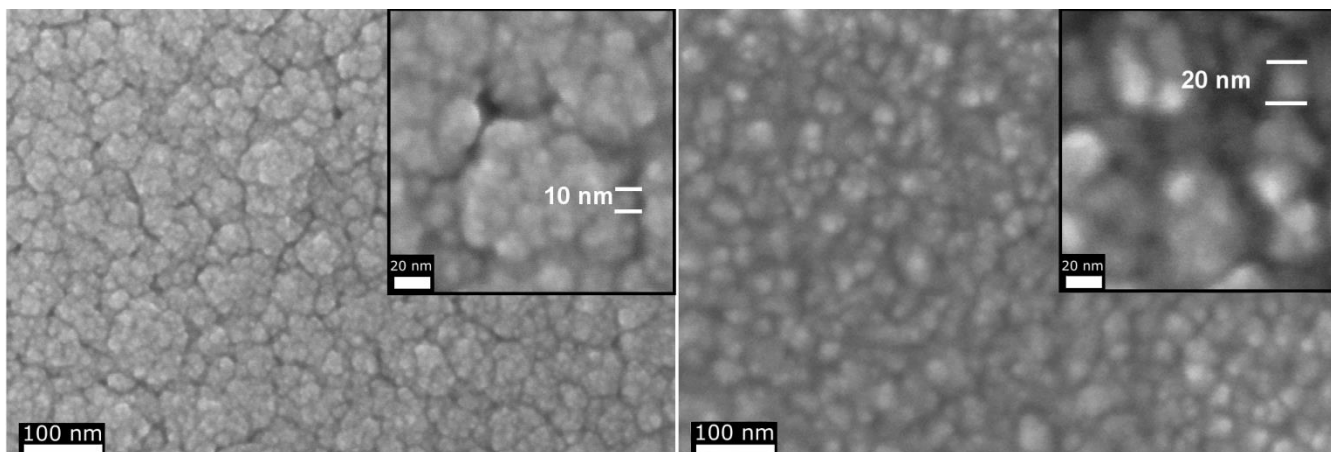
Figure 3: FESEM images of V-doped TiO$_2$ nanoparticle assembled-films on silicon substrates: sample 2 (a) and sample 5 (b) (see Table 1 for samples' specifications). The insets on the top-right corner are the same samples taken at higher magnification. The scale bar is 100 nm / 20 nm for low / high magnification, respectively. The typical NP sizes in the two samples are indicated.

X-ray absorption spectroscopy measurements and data analysis Hard XAS measurements at the Ti and V K – edges were performed at the BM23[45] beamline of the ESRF in Grenoble, France using a double bounce flat crystal Si(111) monochromator. Reference samples (Ti and V oxides) were measured in the transmission mode using finely ground powders dispersed in polyethylene; samples were measured in the fluorescence mode using a Vortex Si drift diode detector placed in the horizontal plane at right angles to the impinging beam. Soft XAS measurements at the Ti and V $L_{2,3}$ – edges were performed at the BACH[46] beamline of Elettra, in Trieste, Italy. In this case, all spectra were collected in the total – electron – yield (TEY) mode, by measuring the drain current from the sample to ground.

EXAFS spectra were processed according to standard procedures using Athena.[47] The pre-edge region was fitted with a linear function while the post – edge region was fitted with a spline to simulate the atomic cross section. As a first approximation the energy origin for the energy – to – wavenumber conversion (E_0) was chosen as the maximum of the first derivative of the absorption spectrum.

Quantitative data analysis was based on simulated signals calculated using the FEFF code[5] and non – linear fitting using ARTEMIS.[36]

In Tab. 1 we report, along with the sample characteristics, the XAS measurements and data analysis performed on the various samples, distinguishing between K and $L_{2,3}$ edges on one hand and XANES and EXAFS on the other. Analysis of the Ti K – edge EXAFS data of the two as – deposited samples will not be reported as these samples were highly disordered and it was not possible to obtain meaningful fits.

Ab-initio simulations. In order to go beyond a qualitative interpretation of the V K-edge XANES spectra, ab-initio calculations were performed. A two – step approach was followed. First of all, we performed a structural relaxation in order to determine the equilibrium atomic coordinates of Ti and O ions around the V dopant using the DFT approach as implemented in the Quantum ESPRESSO code;[48] subsequently, these atomic coordinates were used as an input for full potential spectral simulations with the FDMNES code.[8] Similar or related approaches have been used for studies of dopants and defects in semiconductors.[49–56]

Simulations were performed for anatase and rutile phases, starting from the known crystallographic structures.[57] For both, the pseudopotentials used in structural simulations for Ti, V and O were chosen from the Quantum ESPRESSO database[58–60]. These pseudopotentials are ultra-soft with PBE (Perdew–Burke–Ernzerhof) exchange correlation functional.[61] Self-Consistent Field (SCF) calculations were performed using the Davidson algorithm while the structural relaxations using the BFGS (Broyden-Fletcher-Goldfarb-Shanno) one.[62,63] In order to obtain a realistic simulation of dopant environment at low concentration, it is necessary to build a supercell, composed by several unit cells of the matrix compound. Quantum ESPRESSO automatically replicates this supercell performing calculations with the Plane-Wave Self-Consistent Field algorithm using the PWscf code.[64] The cutoff energy for wavefunctions was set at 30 Ry. An easy way to simulate a realistic environment for a low concentration

dopant is to change only one Ti atom with a V one inside the supercell. After this substitution, the BFGS routine was used to optimize the atomic positions and the supercell dimensions. The k-space sampling for the optimization was done using a $4 \times 4 \times 4$ mesh. SCF convergence was achieved when the difference between the total energy calculated with self-consistent Kohn-Sham DFT and the value calculated with the non self-consistent Harris energy functional[65] was lower than $1.3 \cdot 10^{-6}$ eV. The structural convergence, instead, was achieved when the total force inside the cluster was less than $1 \cdot 10^{-3} \frac{Ry}{a_0}$.

The supercell for rutile was formed by $2 \times 2 \times 3$ tetragonal unit cells, with a total of 72 atoms corresponding to a vanadium-titanium percentage of 4.1%. Inclusion of V in rutile resulted in a compression and distortion of the octahedron formed by the O nearest neighbors; in the basal plane four O atoms relax towards the dopant by ~ 0.03 Å, while the two apical O atoms move inwards by ~ 0.027 Å. The supercell used for anatase was composed by $2 \times 2 \times 2$ unit cells containing 96 atoms corresponding to the substitution of 3.1% of Ti atoms with V ones. Following inclusion of V in anatase the four O nearest neighbors in the basal plane contract inwards by ~ 0.027 Å and the two apical O atoms move inwards by ~ 0.03 Å. The atomic coordinates obtained from the DFT structural relaxations were used as an input for XANES simulations with FDMNES. For the rutile and anatase matrices clusters of 197 and 195 atoms, respectively, were used; they were created using replicas of the Quantum ESPRESSO unit cell. In order to obtain a good correspondence between simulated and experimental spectra in the pre-edge region it was necessary to include quadrupole contributions.

Calculation of the defect formation energy. Starting from Quantum ESPRESSO simulations, we estimated the formation energy of V substitutional defects. In order to do this we firstly calculated the formation energies E_f of the undoped and doped clusters as

$$E_f = E_c - E_i$$

in which E_c is the total energy of the cluster at $T = 0$ and E_i is the sum of all isolated atom energies; the latter was calculated by placing single isolated atoms in a 15 Å simulation cube. Subsequently, we calculated the formation energy of the defect as the difference between the formation energy of the doped and undoped clusters. For the rutile structure we obtain a value of 0.74 eV while for anatase it rises to 1.0 eV. These values are comparable with calculations performed by Osorio-Guillén et al.[66] who provide a complete analysis of the defect formation energy as a function of the Fermi energy of the doped system using the VASP code.
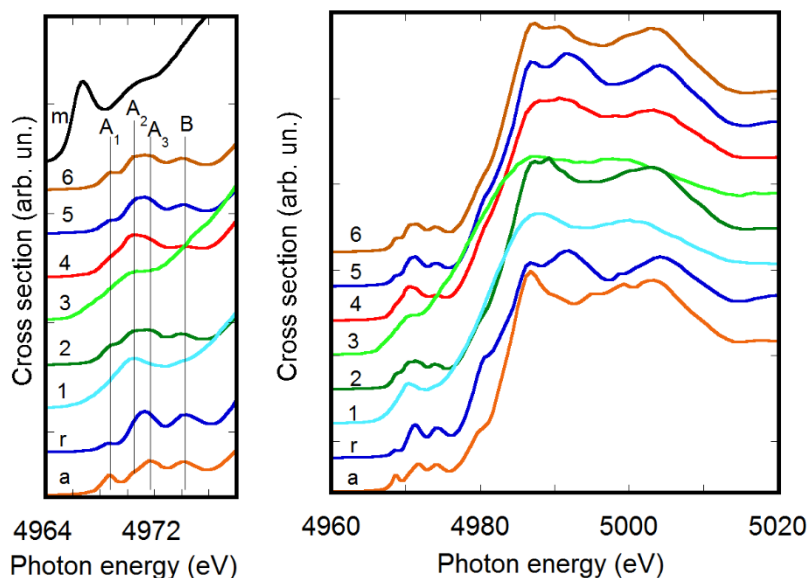
RESULTS AND DISCUSSION

Figure 4. Pre-edge (left) and main edge (right) region of the Ti K-edge XAS in the samples and selected reference compounds.

Local environment of Ti in TiO₂ nanoparticles – the host matrix. In Fig. 4 we report the pre and main edge regions of the Ti *K*-edge XAS spectrum of the samples. By inspection of this data and comparison with the literature[20,22–24,28,30] we may make the following qualitative comments. The as – deposited samples 1 and 3 exhibit a very broad lineshape in both the pre and main edge regions; the onset of the main edge is significantly shifted towards low energy. These observations indicate that these samples are highly disordered and may contain a fraction of metallic Ti. Annealed samples exhibit lineshapes reminiscent of crystalline rutile or anatase. Sample 4, which was annealed at 350 °C, has broader features compared to the others, indicating a poorer degree of ordering. The remaining samples, annealed at 400 °C, exhibit lineshapes that are never identical to rutile or anatase; however, it is noted that sample 2 is more similar to anatase and sample 5 to rutile. This observation suggests that a lower

16

deposition rate, which results in smaller primary NPs, favors the crystallization of anatase. In fact, anatase has a lower surface energy compared to rutile and therefore its formation is preferred at lower nanoparticle sizes.[67] Sample 6 has pre-edge features similar to rutile but an intermediate main edge lineshape. In all these cases the A_2 pre – edge component is more intense than in crystalline oxides; this indicates the presence of under-coordinated, five-fold, Ti ions. Based on these results, we suggest that the V content in the explored range has no or little influence on the relative anatase / rutile phase abundance, which appears to depend mainly on the deposition rate and nanoparticle size.
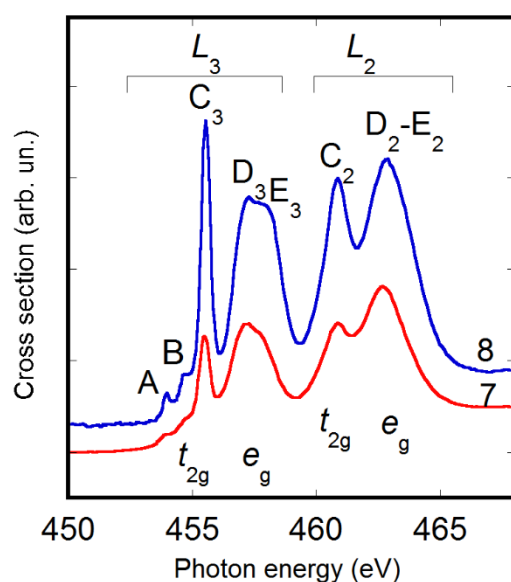

Figure 5. Ti $L_{2,3}$ – edge XAS spectra for as-deposited sample 7 and annealed sample 8.

The qualitative observations deduced from the Ti K – edge spectra are confirmed by $L_{2,3}$ – edge ones. In Fig. 5 we report such spectra for samples 7 and 8, respectively as – deposited and annealed at 400 °C; features related to the L_3 and L_2 edges and to transitions to t_{2g} and e_g orbitals are indicated and individual peaks are labelled as in previous papers[20,21]. Annealing clearly induces a sharpening of spectral features also of the L – edge spectra, a result of greater ordering, in agreement with the EXAFS analysis

(see below). The lineshape of sample 8 spectrum is intermediate between those of rutile and anatase reported in the literature; specifically, the features labelled D_3 and E_3 are approximately of the same intensity while the former is significantly higher than the latter in anatase and the reverse occurs in rutile[18,20]. This confirms that these NP samples exhibit a local structure intermediate between rutile and anatase.
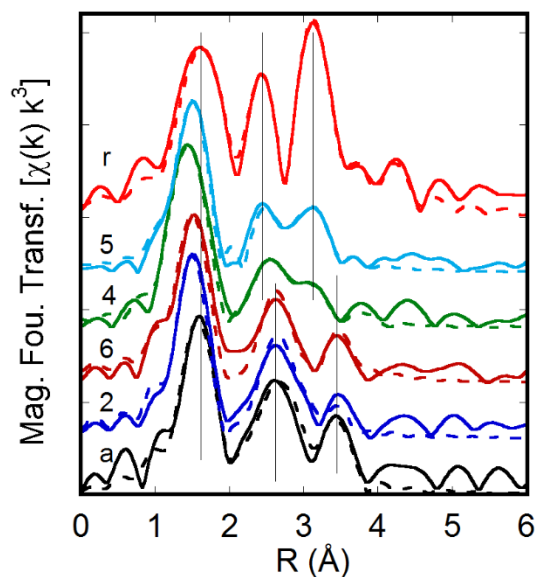

Figure 6. Magnitude of the Fourier Transform of Ti K-edge EXAFS spectra. Solid and dashed lines represent experimental spectra and/ best fits, respectively.

In order to have a quantitative determination of the local structure around Ti we measured and analysed EXAFS spectra. In Fig. 6 we report the magnitude of the Fourier Transform of annealed samples, together with anatase and rutile reference compounds, performed in the range $k = 3.5 - 11$ Å^{-1} with a k^3 weight. The most prominent features in the spectra are due to, in order of increasing distance, the six O nearest neighbors and to Ti atoms in higher coordination shells. Spectra for samples

1 and 3 are not reported and were not analyzed since, as indicated by the qualitative inspection of the XANES spectra, they are very disordered and meaningful fits were not obtained. At a qualitative level, it can be noticed that the spectra of samples are relatively similar and bear some relation either to rutile or anatase. The first shell peak in all samples is found at a slightly smaller distance compared to the reference oxides. Samples 2 and 6 are quite similar to anatase; those of sample 4 and 5 are close to rutile, but with a significantly lower amplitude of the peaks in the region $R = 2 - 4$ Å, an indication of increased structural disorder compared to the crystalline reference. Comparing spectra for sample 4 and 5 (annealed at 350 °C and 400 °C, respectively) it can be noticed that a higher annealing temperature correlates with an increase of the amplitude of the third peak.

For quantitative analysis, the spectra of rutile and anatase were analyzed first. As noted, a state of the art analysis including multiple scattering (MS) contributions is, somewhat surprisingly, not available in the literature. Based on the crystallographic structure the single (SS) and multiple scattering contributions to the fine structure oscillations were calculated using the FEFF code[37]. Using ARTEMIS[36] the spectra were fitted excluding those paths which gave a negligible contribution. Fitting parameters were an energy origin shift, a single isotropic distance variation parameter and individual Debye – Waller (DW) factors for each path. Spectra were fitted in the range $k = 3.5 - 11$ Å^{-1} and $R = 1 - 4$ Å. For anatase we found that the following paths were necessary for a meaningful fit: SS contributions related to the six O nearest neighbors (1st and 2nd shell, fitted as a single component in view of the small distance splitting) and the four Ti ions in the 3rd and 4th coordination shell and a single three - legged MS contribution involving the O nearest neighbors and the Ti in the 4th coordination shell. For rutile SS contributions related to the six O nearest neighbors, the Ti 3rd, O 4th and 5th, Ti 6th, O 7th and 9th shells and three – legged MS contributions related to the O nearest neighbors and the Ti 6th shell were included. Numerical results of fits to anatase and rutile EXAFS spectra are reported in Tables 2 and 3, while the fit themselves are reported as dashed lines in Fig. 6.

Table 2: Numerical results of fits for anatase and samples 2 and 6. Numbers in brackets indicate uncertainties in best estimates.

path	legs	N	anatase R (Å)	anatase σ^2 (Å^2)	2 R (Å)	2 σ^2 (Å^2)	6 R (Å)	6 σ^2 (Å^2)
O (1st/2nd)	2	6	1.9565 (99)	0.0055 (12)	1.9321 (96)	0.0045 (13)	1.948 (20)	0.0065 (19)
Ti (3rd)	2	4	3.055 (15)	0.0058 (12)	3.048 (12)	0.0078 (13)	3.061 (40)	0.0071 (20)
Ti (4th)	2	4	3.804 (19)	0.0040 (31)	3.720 (76)	0.0063 (34)	3.680 (76)	0.0058 (34)
O (1st/2nd) Ti (4th)	3	8	3.849 (20)	0.0075 (17)	3.780 (30)	0.0153 (41)	3.791 (18)	0.0038 (30)

Table 3: Numerical results of fits for rutile and samples 4 and 5. Numbers in brackets indicate uncertainties in best estimates.

path	legs	N	rutile R (Å)	rutile σ^2 (Å^2)	4 R (Å)	4 σ^2 (Å^2)	5 R (Å)	5 σ^2 (Å^2)
O (1st/2nd)	2	6	1.9636 (74)	0.0080 (17)	1.946 (20)	0.0079 (38)	1.952 (13)	0.0075 (21)
Ti (3rd)	2	2	2.9656 (11)	0.0039 (18)	3.047 (40)	0.0059 (71)	3.040 (30)	0.0058 (37)
O (4th)	2	4	3.495 (13)	0.0000 (40)	–	–	–	–
O (5th)	2	4	3.568 (14)	0.0115 (18)	–	–	–	–
Ti (6th)	2	8	3.578 (14)	0.0095 (44)	3.60 (22)	0.021 (81)	3.556 (22)	0.015 (79)
O (1st/2nd) Ti (6th)	3	16	3.758 (14)	0.0015 (31)	3.69 (42)	0.001 (39)	3.66 (17)	0.000 (13)
O (7th)	2	8	4.091 (15)	0.020 (24)	3.866 (90)	0.000 (17)	3.819 (89)	0.008 (41)
O (9th)	2	8	4.584 (15)	0.0038 (29)	–	–	–	–

The EXAFS spectra of the samples were fitted using either the paths used for rutile or anatase. The choice of which paths to use was based on the similarity of the XANES pre – edge and main edge features to the reference compounds. This procedure must be taken with some caution since the local structure of

a NP is never identical to that of a bulk coarse grained crystal; also, the XANES lineshapes of the samples are never identical to either reference compound. The path degeneracies were kept fixed at the values of the crystals since, due to the well known high correlation with Debye – Waller factors, it was impossible to determine them with a reasonable uncertainty. For samples 4 and 5 some of the weak O contributions were not included, as their structural parameters could not be determined reliably. The numerical results of the fits are reported in Tabs. 2 and 3 and the fits themselves, of good quality, are reported as the dashed lines in Fig. 6. Despite the somewhat relatively high uncertainties, overall, the numerical values confirm the qualitative comments made above on Fig. 6. For anatase – like samples, the DW factors for the Ti coordination shells are slightly higher than in the reference. For rutile – like samples, the same trend is found; sample 4, annealed at a lower temperature, has the highest DW for the Ti – Ti 6th coordination shell. The Ti – O first shell interatomic distances in the NPs are shorter than in the reference compounds by 0.01 – 0.02 Å.

Local environment of V dopants in TiO₂ nanoparticles: XAFS spectra at the V K and $L_{2,3}$ edges were measured with the aim of determining the incorporation site of V in the TiO₂ NPs. At the K edge, due to the overlap of the Ti K_β and V K_α fluorescence lines it proved impossible to measure EXAFS spectra with good signal – to – noise ratio. However, good quality XANES spectra were recorded. These spectra, along with those for V_2O_3, VO_2 and V_2O_5 reference compounds are reported in Fig. 7; the oxides are plotted in order of increasing oxidation state of V from bottom to top (3+, 4+ and 5+), recalling the relation between energy of spectral features and oxidation state[29,30,32,68]. We also report the rutile and anatase spectra shifted by + 500 eV (energy difference between V and Ti K edges) as a comparison. In Fig. 8 the derivatives of the spectra for annealed samples and reference compounds are reported, to allow a more detailed comparison.
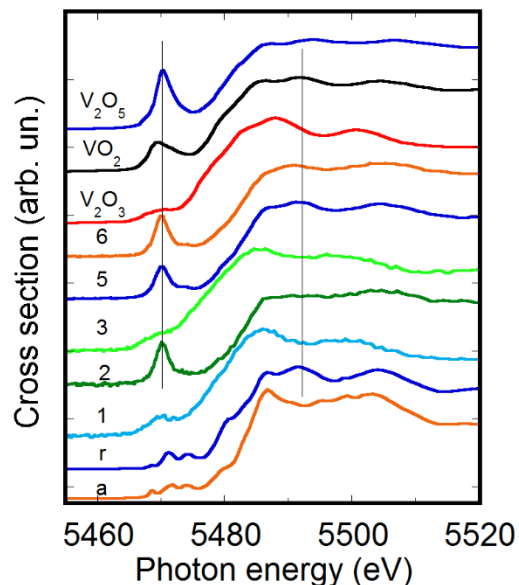
Figure 7. V *K* edge XANES of selected samples and reference compounds. Also reported are the Ti *K* edge

spectra of rutile and anatase shifted by + 500 eV. The vertical lines are guides to the eye.
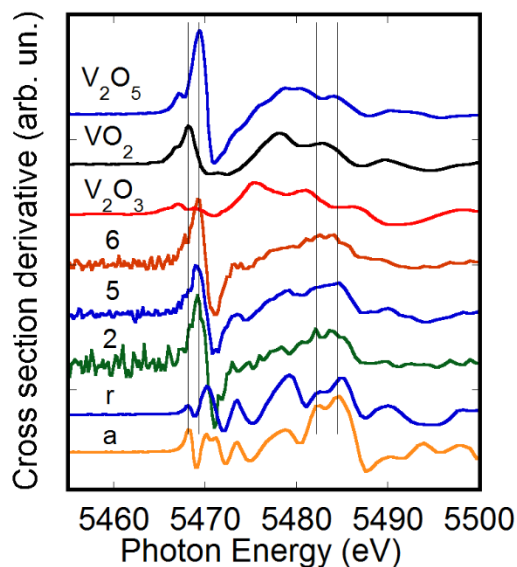

Figure 8. Derivatives of the spectra presented in Fig. 7.

Firstly, we note that as – deposited samples 1 and 3 exhibit broad spectral features, indicating a

rather disordered V environment, in analogy to the Ti environment in the oxide NP matrix, as described

previously. Annealing induces a sharpening of spectral features and a shift to higher energy of the main

edge, as also found at the Ti edge. In annealed samples 2, 5 and 6, the pre – edge region is characterized

22

by a sharp peak and a weak shoulder at higher photon energy. These pre – edge features, due to dipole and quadrupole transitions to bound hybridized orbitals originating from O p and V d atomic ones, are reminiscent of the pre – edge peak features of V_2O_5; the intensity of the pre – edge peak in the samples is, however, less than in V_2O_5. The main edge features of the spectra do not bear a strong correspondence to those of V_2O_5; especially significant is the energy onset of the main edge, which is significantly shifted to higher energies in the samples with respect to the reference V oxides. The closest (albeit not complete) correspondence is between spectra of sample 2 and anatase on one hand and, especially, between sample 5 and rutile on the other. Recall that analysis of the Ti edge XANES and EXAFS indicated a local Ti environment similar to anatase in sample 2 and similar to rutile in sample 5. For sample 6, the Ti XANES pre and main edge features indicated a mixed environment and this has a correspondence with the V K edge spectrum. The V edge data therefore strongly suggest that V substitutionally occupies a Ti site in the NP matrix, irrespective of whether it is similar to rutile, anatase or mixed. Regarding the oxidation state, a conclusive result is difficult to reach with certainty since pre – edge and XANES lineshapes depend on the oxidation state of the absorber, its local point symmetry and the elemental composition of its first coordination shells. Thus, it is not possible to rigorously compare spectra of V oxide reference compounds and of samples in which an isolated V is surrounded by a TiO_2 matrix. The coincidence of the energy position of the pre – edge peak of the samples with that of V_2O_5 suggests an oxidation state close to 5+. However its intensity, intermediate between those of V_2O_5 and VO_2 pre-edge peaks, is also compatible with the presence of V^{4+} ions. A mixed oxidation state may arise from V occupying both bulk-like and surface-like sites in the NPs. In bulk-like sites, the most stable V oxidation state is 4+,[41] because its associated donor transition level lies deep in the TiO_2 gap[3,66]. On the other hand, surface V ions may attain the 5+ oxidation state, most stable under oxygen-rich conditions. In the present case, due to the small NPs size coupled with the positive energy of formation of the substitutional cationic defect, significant surface enrichment by V may be expected. In V-doped TiO_2 NPs prepared by chemical

23

methods, the formation of V^{5+} vanadate surface-cluster species for V contents higher than about 5% was reported[2,41]. Surface enrichment by V^{5+} ions, which implies a stronger contribution from surface-like sites to the V K edge spectra, may also account for the differences observed between the V K edge and the shifted Ti K edge XANES of nanoparticle-assembled films.

Besides contributing to band-gap narrowing, V^{4+} ions can trap both electrons and holes, thus favoring charge separation and enhancing visible-light photo-catalytic activity.[41] In addition, V^{5+} surface species were reported to scavenge photo-generated electrons from TiO_2 and to facilitate their transfer to oxygen molecules on the NPs surface, eventually forming superoxide radicals active in the degradation of toxic dyes.[2]

The sharpening of spectral features upon annealing and the blue-shift of V – related ones are also evident from combined V $L_{2,3}$ and O K edge XANES spectra, reported in Fig. 9. The lineshapes of the O K edge spectra, in comparison to the literature[20,21], indicate once more a local structure intermediate between rutile and anatase for annealed sample 8.
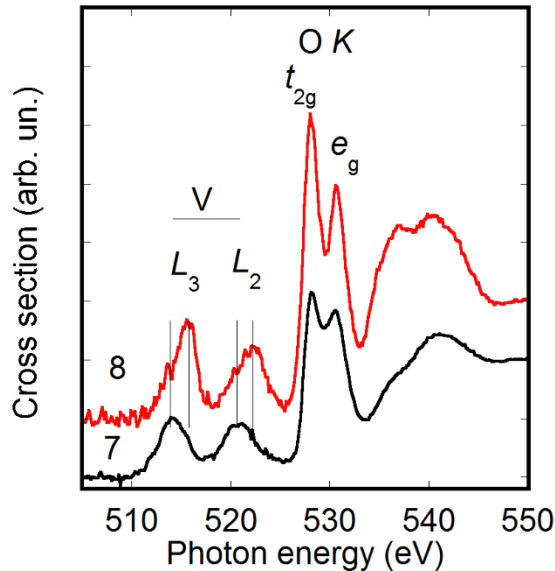
Figure 9. V $L_{2,3}$ and O K edge XANES spectra in as-deposited sample 7 and annealed sample 8.

In order to put the above qualitative observations on a firm ground, *ab-initio* calculations of the XANES spectra of V-doped TiO_2 in rutile and anatase structures were performed, using the approach described above. Comparisons between simulations and selected experimental spectra are reported in Fig. 10, following convolution with an arctangent function. Simulated spectra have been shifted a few eV's in order to align the first pre – edge peak. Overall, the comparison is very convincing. In both cases, the pre – edge peak is correctly simulated. The main edge part of the spectrum simulated in the rutile matrix corresponds quite well to that of sample 5, although the two features at 5487 and 5492 eV merge into a single one in the simulations; the correspondence of the simulated spectra for the anatase matrix and sample 2 is fair, especially if we recall that the local structure of the matrix in sample 2 is not ideal anatase. The ab-initio simulations thus confirm the indications obtained from the qualitative inspection of the XANES spectra.
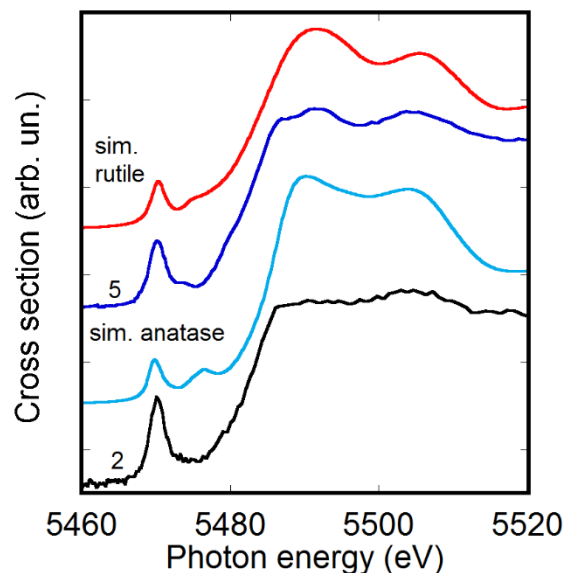
Figure 10. V *K* edge XANES spectra for samples 2 and 5 and simulations for a substitutional V cation in rutile and anatase lattices.

CONCLUSIONS

In conclusion, we have reported an in-depth study of the location of V dopants in TiO_2 NPs with different anatase / rutile relative abundance prepared by gas-phase condensation. By measuring *K* and *L* edge spectra in the pre-edge, XANES and EXAFS regions and combining analysis of the experimental spectra with full potential *ab-initio* simulations of the XANES lineshape, we show that V ions occupy substitutional cationic sites in the TiO_2 matrix, irrespective of whether it is similar to rutile, anatase or mixed. Therefore, gas-phase condensation is a viable technique to grow nanoparticle-assembled metal-ion doped TiO_2 films with an anatase-to-rutile ratio that can be tuned by adjusting the evaporation parameters. The positive formation energy of the cationic substitutional defect, coupled with the small NPs size, shall result in a dopant-enriched NPs surface. In fact, the V *K* pre-edge features are compatible

with the presence of both V^{4+} and V^{5+} oxidation states, the former being likely associated with bulk-like sites inside the NPs, the latter with surface sites.

References

(1) Fujishima, A.; Zhang, X.; Tryk, D. A. TiO2 Photocatalysis and Related Surface Phenomena. *Surf. Sci. Rep.* **2008**, *63* (12), 515–582.

(2) Jaiswal, R.; Patel, N.; Kothari, D. C.; Miotello, A. Improved Visible Light Photocatalytic Activity of TiO2 Co-Doped with Vanadium and Nitrogen. *Appl. Catal. B Environ.* **2012**, *126*, 47–54.

(3) Umebayashi, T.; Yamaki, T.; Itoh, H.; Asai, K. Analysis of Electronic Structures of 3d Transition Metal-Doped TiO2 Based on Band Calculations. *J. Phys. Chem. Solids* **2002**, *63* (10), 1909–1920.

(4) Asahi, R.; Morikawa, T.; Ohwaki, T.; Aoki, K.; Taga, Y. Visible-Light Photocatalysis in Nitrogen-Doped Titanium Oxides. *Science* **2001**, *293* (5528), 269–271.

(5) Zabinsky, S. I.; Rehr, J. J.; Ankudinov, A.; Albers, R. C.; Eller, M. J. Multiple-Scattering Calculations of X-Ray-Absorption Spectra. *Phys. Rev. B* **1995**, *52* (4), 2995–3009.

(6) Filipponi, A.; Di Cicco, A.; Natoli, C. R. X-Ray-Absorption Spectroscopy and n-Body Distribution Functions in Condensed Matter. I. Theory. *Phys. Rev. B* **1995**, *52* (21), 15122–15134.

(7) Filipponi, A.; Di Cicco, A. X-Ray-Absorption Spectroscopy and n-Body Distribution Functions in Condensed Matter. II. Data Analysis and Applications. *Phys. Rev. B* **1995**, *52* (21), 15135–15149.

(8) Bunău, O.; Joly, Y. Self-Consistent Aspects of X-Ray Absorption Calculations. *J. Phys. Condens. Matter* **2009**, *21* (34), 345501.

(9) Joly, Y.; Cabaret, D.; Renevier, H.; Natoli, C. R. Electron Population Analysis by Full-Potential X-Ray Absorption Simulations. *Phys. Rev. Lett.* **1999**, *82* (11), 2398–2401.

(10) Signorini, L.; Pasquini, L.; Savini, L.; Carboni, R.; Boscherini, F.; Bonetti, E.; Giglia, A.; Pedio, M.; Mahne, N.; Nannarone, S. Size-Dependent Oxidation in Iron/Iron Oxide Core-Shell Nanoparticles. *Phys. Rev. B* **2003**, *68* (19), 195423.

(11) Boscherini, F. In *X-ray Absorption Spectroscopy of Semiconductors*; Schnor, C.S., Ridgway, M., Eds.; 2015.

(12) Boscherini, F. In *Characterization of Semiconductor Heterostructures and Nanostructures*; Lamberti, C., Agostini, G., Eds.; 2013.

(13) Boscherini, F. In *Synchrotron Radiation: Basics, Methods and Applications*; Boscherini, F., Meneghini, C., Mobilio, S., Eds; 2015.

(14) Yamamoto, T. Assignment of Pre-Edge Peaks in K-Edge X-Ray Absorption Spectra of 3d Transition Metal Compounds: Electric Dipole or Quadrupole? *X-Ray Spectrom.* **2008**, *37* (6), 572–584.

(15) Glatzel, P.; Sikora, M.; Fernández-García, M. Resonant X-ray Spectroscopy to Study K Absorption Pre-Edges in 3d Transition Metal Compounds. *Eur. Phys. J. Spec. Top.* **2009**, *169* (1), 207–214.

(16) Farges, F.; Brown, G. E.; Rehr, J. J. Ti K-edge XANES Studies of Ti Coordination and Disorder in Oxide Compounds: Comparison between Theory and Experiment. *Phys. Rev. B* **1997**, *56* (4), 1809–1819.

(17) Bohr, F.; Ruiz-López, M. F.; Muñoz-Páez, A. A Multiple-Scattering Approach to the Study of X-ray Absorption Spectra of Anatase and Rutile. *Catal. Lett.* **1993**, *20* (1-2), 59–71.

(18) Groot, F. M. F. de; Figueiredo, M. O.; Basto, M. J.; Abbate, M.; Petersen, H.; Fuggle, J. C. 2p X-ray Absorption of Titanium in Minerals. *Phys. Chem. Miner.* **1992**, *19* (3), 140–147.

(19) Lucovsky, G.; Whitten, J. L.; Zhang, Y. A Molecular Orbital Model for the Electronic Structure of Transition Metal Atoms in Silicate and Aluminate Alloys. *Microelectron. Eng.* **2001**, *59* (1–4), 329–334.

(20) Kucheyev, S. O.; van Buuren, T.; Baumann, T. F.; Satcher, J. H.; Willey, T. M.; Meulenberg, R. W.; Felter, T. E.; Poco, J. F.; Gammon, S. A.; Terminello, L. J. Electronic Structure of Titania Aerogels from Soft X-Ray Absorption Spectroscopy. *Phys. Rev. B* **2004**, *69* (24), 245102.

(21) Stewart, S. J.; Fernández-García, M.; Belver, C.; Mun, B. S.; Requejo, F. G. Influence of N-Doping on the Structure and Electronic Properties of Titania Nanoparticle Photocatalysts. *J. Phys. Chem. B* **2006**, *110* (33), 16482–16486.

(22) Hanley, T. L.; Luca, V.; Pickering, I.; Howe, R. F. Structure of Titania Sol−Gel Films: A Study by X-Ray Absorption Spectroscopy. *J. Phys. Chem. B* **2002**, *106* (6), 1153–1160.

(23) Luca, V.; Djajanti, S.; Howe, R. F. Structural and Electronic Properties of Sol−Gel Titanium Oxides Studied by X-ray Absorption Spectroscopy. *J. Phys. Chem. B* **1998**, *102* (52), 10650–10657.

(24) Luca, V. Comparison of Size-Dependent Structural and Electronic Properties of Anatase and Rutile Nanoparticles. *J. Phys. Chem. C* **2009**, *113* (16), 6367–6380.

(25) Chen, L. X.; Rajh, T.; Wang, Z.; Thurnauer, M. C. XAFS Studies of Surface Structures of TiO2 Nanoparticles and Photocatalytic Reduction of Metal Ions. *J. Phys. Chem. B* **1997**, *101* (50), 10688–10697.

(26) Li, W.; Frenkel, A. I.; Woicik, J. C.; Ni, C.; Shah, S. I. Dopant Location Identification in Nd^{3+}-Doped TiO_2 Nanoparticles. *Phys. Rev. B* **2005**, *72* (15), 155315.

(27) Rodríguez-Torres, C. E.; Cabrera, A. F.; Errico, L. A.; Adán, C.; Requejo, F. G.; Weissmann, M.; Stewart, S. J. Local Structure and Magnetic Behaviour of Fe-Doped TiO 2 Anatase Nanoparticles: Experiments and Calculations. *J. Phys. Condens. Matter* **2008**, *20* (13), 135210.

(28) Marchiori, C.; Di Liberto, G.; Soliveri, G.; Loconte, L.; Lo Presti, L.; Meroni, D.; Ceotto, M.; Oliva, C.; Cappelli, S.; Cappelletti, G.; et al. Unraveling the Cooperative Mechanism of Visible-Light Absorption in Bulk N,Nb Codoped TiO2 Powders of Nanomaterials. *J. Phys. Chem. C* **2014**, *118* (41), 24152–24164.

(29) Bianconi, A. Multiplet Splitting of Final-State Configurations in X-Ray-Absorption Spectrum of Metal VO2: Effect of Core-Hole-Screening, Electron Correlation, and Metal-Insulator Transition. *Phys. Rev. B* **1982**, *26* (6), 2741–2747.

(30) Wong, J.; Lytle, F. W.; Messmer, R. P.; Maylotte, D. H. K-Edge Absorption Spectra of Selected Vanadium Compounds. *Phys. Rev. B* **1984**, *30* (10), 5596–5610.

(31) Giuli, G.; Paris, E.; Mungall, J.; Romano, C.; Dingwell, D. V Oxidation State and Coordination Number in Silicate Glasses by XAS. *Am. Mineral.* **2004**, *89* (11-12), 1640–1646.

(32) Sutton, S. R.; Karner, J.; Papike, J.; Delaney, J. S.; Shearer, C.; Newville, M.; Eng, P.; Rivers, M.; Dyar, M. D. Vanadium K Edge XANES of Synthetic and Natural Basaltic Glasses and Application to Microscale Oxygen Barometry. *Geochim. Cosmochim. Acta* **2005**, *69* (9), 2333–2348.

(33) Izumi, Y.; Kiyotaki, F.; Yoshitake, H.; Aika, K.; Sugihara, T.; Tatsumi, T.; Tanizawa, Y.; Shido, T.; Iwasawa, Y. Structure of Low Concentrations of Vanadium on TiO2 Determined by XANES and Ab Initio Calculations. *Chem. Commun.* **2002**, No. 20, 2402–2403.

(34) Avansi, W.; Arenal, R.; de Mendonça, V. R.; Ribeiro, C.; Longo, E. Vanadium-Doped TiO2 Anatase Nanostructures: the Role of V in Solid Solution Formation and its Effect on the Optical Properties. *CrystEngComm* **2014**, *16* (23), 5021.

(35) Nagaveni, K.; Hegde, M. S.; Madras, G. Structure and Photocatalytic Activity of Ti1-xMxO2±δ (M = W, V, Ce, Zr, Fe, and Cu) Synthesized by Solution Combustion Method. *J. Phys. Chem. B* **2004**, *108* (52), 20204–20212.

(36) Rittmann-Frank, M. H.; Milne, C. J.; Rittmann, J.; Reinhard, M.; Penfold, T. J.; Chergui, M. Mapping of the Photoinduced Electron Traps in TiO2 by Picosecond X-Ray Absorption Spectroscopy. *Angew. Chem. Int. Ed.* **2014**, *53* (23), 5858–5862.

(37) Amidani, L.; Naldoni, A.; Malvestuto, M.; Marelli, M.; Glatzel, P.; Del Santo, V.; Boscherini, F. Probing Long-Lived Plasmonic-Generated Charges in TiO2/Au by High-Resolution X-Ray Absorption Spectroscopy. *Angew. Chem. Int. Ed.* **2015**, *54*, 5413–5416.

(38) Pasquini, L.; Sacchi, M.; Boelsma, C.; Bals, S.; Perkisas, T.; Dam, B. Hydride Destabilization in Core-Shell Nanoparticles. *Int. J. Hydrog. ENERGY* **2014**, *39*, 2115–2123.

(39) FactSage Browser - online http://www.crct.polymtl.ca/FACT/documentation/ (accessed Dec 4, 2015).

(40) Wood, D. L.; Tauc, J. Weak Absorption Tails in Amorphous Semiconductors. *Phys. Rev. B* **1972**, *5* (8), 3144–3151.

(41) Kubacka, A.; Fuerte, A.; Martínez-Arias, A.; Fernández-García, M. Nanosized Ti–V Mixed Oxides: Effect of Doping Level in the Photo-Catalytic Degradation of Toluene Using Sunlight-Type Excitation. *Appl. Catal. B Environ.* **2007**, *74* (1–2), 26–33.

(42) Liu, J.; Han, R.; Zhao, Y.; Wang, H.; Lu, W.; Yu, T.; Zhang, Y. Enhanced Photoactivity of V−N Codoped TiO2 Derived from a Two-Step Hydrothermal Procedure for the Degradation of PCP−Na under Visible Light Irradiation. *J. Phys. Chem. C* **2011**, *115* (11), 4507–4515.

(43) Chang, S.; Liu, W. Surface Doping is More Beneficial than Bulk Doping to the Photocatalytic Activity of Vanadium-Doped TiO2. *Appl. Catal. B Environ.* **2011**, *101* (3–4), 333–342.

(44) Pasquini, L.; Barla, A.; Chumakov, A. I.; Leupold, O.; Rüffer, R.; Deriu, A.; Bonetti, E. Size and Oxidation Effects on the Vibrational Properties of Nanocrystalline α-Fe. *Phys. Rev. B* **2002**, *66* (7), 073410.

(45) BM23 - XAS beamline http://www.esrf.eu/UsersAndScience/Experiments/MEx/BM23 (accessed Dec 4, 2015).

(46) Elettra Sincrotrone Trieste http://www.elettra.eu/elettra-beamlines/bach.html (accessed Dec 4, 2015).

(47) Ravel, B.; Newville, M. *ATHENA* , *ARTEMIS* , *HEPHAESTUS* : Data Analysis for X-Ray Absorption Spectroscopy Using *IFEFFIT*. *J. Synchrotron Radiat.* **2005**, *12* (4), 537–541.

(48) Giannozzi, P.; Baroni, S.; Bonini, N.; Calandra, M.; Car, R.; Cavazzoni, C.; Davide Ceresoli; Chiarotti, G. L.; Cococcioni, M.; Dabo, I.; et al. QUANTUM ESPRESSO: a Modular and Open-Source Software Project for Quantum Simulations of Materials. *J. Phys. Condens. Matter* **2009**, *21* (39), 395502.

(49) Berti, M.; Bisognin, G.; De Salvador, D.; Napolitani, E.; Vangelista, S.; Polimeni, A.; Capizzi, M.; Boscherini, F.; Ciatto, G.; Rubini, S.; et al. Formation and Dissolution of D-N Complexes in Dilute Nitrides. *Phys. Rev. B* **2007**, *76* (20), 205323.

(50) Ciatto, G.; Boscherini, F.; Amore Bonapasta, A.; Filippone, F.; Polimeni, A.; Capizzi, M.; Berti, M.; Bisognin, G.; De Salvador, D.; Floreano, L.; et al. Local Structure of Nitrogen-Hydrogen Complexes in Dilute Nitrides. *Phys. Rev. B* **2009**, *79* (16), 165205.

(51) Katsikini, M.; Boscherini, F.; Paloura, E. C. Local Bonding Geometry of Oxygen Implanted in GaN: A Depth-Dependent Study. *J. Nanosci. Nanotechnol.* **2010**, *10* (9), 6260–6265.

(52) Boscherini, F.; D'Acapito, F.; Galata, S. F.; Tsoutsou, D.; Dimoulas, A. Atomic Scale Mechanism for the Ge-Induced Stabilization of the Tetragonal, Very High-κ, Phase of ZrO2. *Appl. Phys. Lett.* **2011**, *99* (12), 121909.

(53) d'Acapito, F. Advanced Methods for the Analysis of X-Ray Absorption Spectroscopy Data Applied to Semiconductors. *Semicond. Sci. Technol.* **2011**, *26* (6), 064004.

(54) Amidani, L.; Filippone, F.; Amore Bonapasta, A.; Ciatto, G.; Lebedev, V.; Knübel, A.; Boscherini, F. X-ray Absorption Spectra of $In_xGa_{1-x}N$ Alloys with Insight from Atom-Specific Simulations. *Phys. Rev. B* **2012**, *86* (15), 155211.

(55) De Luca, M.; Pettinari, G.; Ciatto, G.; Amidani, L.; Filippone, F.; Polimeni, A.; Fonda, E.; Boscherini, F.; Bonapasta, A. A.; Giubertoni, D.; et al. Identification of Four-Hydrogen Complexes in In-Rich $In_xGa_{1-x}N$ (x>0.4) Alloys Using Photoluminescence, X-Ray Absorption, and Density Functional Theory. *Phys. Rev. B* **2012**, *86* (20), 201202.

(56) Amidani, L.; Ciatto, G.; Boscherini, F.; Filippone, F.; Mattioli, G.; Alippi, P.; Bondino, F.; Polimeni, A.; Capizzi, M.; Amore Bonapasta, A. Connections Between Local and Macroscopic Properties in Solids: The Case of N in III-V-N Alloys. *Phys. Rev. B* **2014**, *89* (8), 085301.

(57) Wyckoff, R. W. G. *Crystal Structures.*; New York, Interscience; 1960; Vol. 1.

(58) Kohlmeyer, A. O.pbe-van_ak.UPF http://www.quantum-espresso.org/wp-content/uploads/upf_files/O.pbe-van_ak.UPF (accessed Jan 14, 2016).

(59) Kohlmeyer, A. Ti.pbe-sp_van_ak.UPF http://www.quantum-espresso.org/pseudo/1.3/UPF/Ti.pbe-sp-van_ak.UPF (accessed Jan 14, 2016).

(60) Seng Wu, H. V.pbe-sp-van.UPF http://www.quantum-espresso.org/wp-content/uploads/upf_files/V.pbe-sp-van.UPF (accessed Jan 14, 2016).

(61) Perdew, J. P.; Burke, K.; Ernzerhof, M. Generalized Gradient Approximation Made Simple. *Phys. Rev. Lett.* **1996**, *77* (18), 3865–3868.

(62) Avriel, M. *Nonlinear Programming: Analysis and Methods*, Dover Publishing.; 2003.

(63) Broyden, C. G. The Convergence of a Class of Double-rank Minimization Algorithms 1. General Considerations. *IMA J. Appl. Math.* **1970**, *6* (1), 76–90.

(64) PWscf User's Guide http://www.quantum-espresso.org/wp-content/uploads/Doc/pw_user_guide.pdf.

(65) Harris, J. Simplified Method for Calculating the Energy of Weakly Interacting Fragments. *Phys. Rev. B* **1985**, *31* (4), 1770–1779.

(66) Osorio-Guillén, J.; Lany, S.; Zunger, A. Atomic Control of Conductivity Versus Ferromagnetism in Wide-Gap Oxides Via Selective Doping: V, Nb, Ta in Anatase TiO_2. *Phys. Rev. Lett.* **2008**, *100* (3), 036601.

(67) Hanaor, D. A. H.; Sorrell, C. C. Review of the Anatase to Rutile Phase Transformation. *J. Mater. Sci.* **2010**, *46* (4), 855–874.

(68) Whittaker, L.; Wu, T.-L.; Patridge, C. J.; Sambandamurthy, G.; Banerjee, S. Distinctive Finite Size Effects on the Phase Diagram and Metal–Insulator Transitions of Tungsten-Doped Vanadium(IV) Oxide. *J. Mater. Chem.* **2011**, *21* (15), 5580–5592.
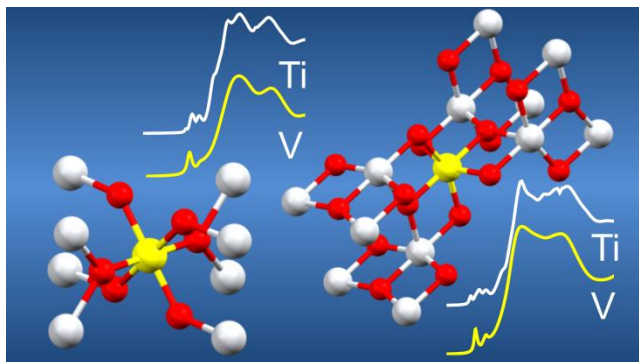
TOC image

Substitutional vanadium atoms in TiO_2 rutile and anatase structures show XANES spectra comparable with the non-doped ones